Mon. Not. R. Astron. Soc. **000**, 1–10 () Printed 5 February 2008 (MN LATEX style file v2.2)

On the γ-ray emission of Type Ia Supernovae

S. A. Sim[1], P. A. Mazzali[1,2,3]
[1]*Max-Planck-Institut für Astrophysik, Karl-Schwarzschildstr. 1, 85748 Garching, Germany*
[2]*Istituto Nazionale di Astrofisica-Osservatorio Astronomico di Trieste, Via Tiepolo 11, I-34131 Trieste, Italy*
[3]*Kavli Institute for Theoretical Physics, University of California, Santa Barbara, CA 93106*

25 Oct 2007

ABSTRACT
A multi-dimension, time-dependent Monte Carlo code is used to compute sample γ-ray spectra to explore whether unambiguous constraints could be obtained from γ-ray observations of type Ia supernovae. Both spherical and aspherical geometries are considered and it is shown that moderate departures from sphericity can produce viewing-angle effects that are at least as significant as those caused by the variation of key parameters in one-dimensional models. Thus γ-ray data could in principle carry some geometrical information, and caution should be applied when discussing the value of γ-ray data based only on one-dimensional explosion models. In light of the limited sensitivity of current γ-ray observatories, the computed theoretical spectra are studied to revisit the issue of whether useful constraints could be obtained for moderately nearby objects. The most useful γ-ray measurements are likely to be of the light curve and time-dependent hardness ratios, but sensitivity higher than currently available, particularly at relatively hard energies ($\sim 2-3$ MeV), is desirable.

Key words: radiative transfer – methods: numerical – supernovae: general

1 INTRODUCTION

Although the paradigm that Type Ia supernovae (SNe Ia) result from the explosions of carbon-oxygen white dwarfs is well established, many issues regarding the nature of the progenitors and the explosion mechanism remain unclear (see e.g. Hillebrandt & Niemeyer 2000). Achieving a clearer understanding of SNe Ia is important because of their role in the chemical evolution of galaxies and as cosmological distance indicators.

Considerable theoretical effort has gone into modelling of SNe Ia explosions. Recently, fully three-dimensional (3D) modelling of the explosion (Reinecke et al. 2002; Gamezo et al. 2003; Röpke & Hillebrandt 2005; Röpke et al. 2006; Jordan et al. 2007) has become feasible, allowing a detailed treatment of the hydrodynamical instabilities and turbulence which play a pivotal role. The 3D structure predicted by these models has been shown to affect observables such as optical/ultra-violet/infrared (UVOIR) light curves and spectra (e.g. Kasen & Plewa 2006; Sim 2007; Sim et al. 2007).

Although they are primarily detected through their optical emission, SNe Ia are also expected to be γ-ray sources owing to the large masses of radioactive isotopes synthesised in the explosion (e.g. Travaglio et al. 2004). In principle, measurements of γ-ray emission from SNe Ia could provide important diagnostics since γ rays trace almost directly the mass and velocity distribution of the products of nuclear burning. Therefore, there has been considerable theoretical work on SN Ia γ-ray emission (e.g. Ambwani & Sutherland 1988; Burrows & The 1990; Müller et al. 1991; Höflich et al. 1992; Kumagai & Nomoto 1997; Höflich et al. 1998; Gómez-Gomar et al. 1998; Milne et al. 2004). Unfortunately, owing to the low sensitivity of γ-ray observatories, to date only one SN Ia (SN1991T) has been detected (see discussion by Milne et al. 2004). However, with current instrumentation such as the *SPI* (Vedrenne et al. 2003) on-board *Integral* (Winkler et al. 2003), detection of SN Ia within several Mpc would be possible (Gómez-Gomar et al. 1998). Moreover, increased sensitivity in future missions should make detection feasible for more distant SNe Ia.

Most studies of SN Ia γ-ray emission focus on making predictions from individual models representing specific explosion mechanisms. In general, these studies have been restricted to one-dimension (although see Höflich & Stein 2002) and to Chandrasekhar-mass models (some sub-Chandrasekhar models have been considered, e.g. Höflich et al. 1998; Gómez-Gomar et al. 1998). Such studies demonstrated that, for nearby SN Ia, the prospects of obtaining useful data are fairly good. Here we adopt a different but complementary approach, motivated by the increasing variety of explosion conditions suggested (both in theoretical and semi-empirical studies): rather than determining the quality of γ-ray data that would be needed to distinguish specific models, we attempt to show what might be unambiguously determined solely from data and the physics of γ-ray radiation transport.

We use a multi-dimensional, time-dependent code to compute γ-ray spectra for a set of parameterised geometries spanning a broad range in the relevant physical conditions. Using these reference spectra, we highlight the quantities that would be most useful diagnostics and therefore most worthy of consideration in the design of future instrumentation.

In Section 2, we briefly describe the code used to compute the reference γ-ray spectra. The reference models we employ are motivated in Section 3 and their spectra are discussed in Section 4. Guided by our reference spectra, in Section 5 we examine observational diagnostics. Finally, in Section 6, we summarise our results.

2 RADIATIVE TRANSFER CALCULATIONS

Our calculations were performed using Monte Carlo methods to track the emission, propagation, scattering and absorption of quanta which represent bundles of γ-ray photons. Monte Carlo methods are widely used in modelling γ-ray spectra for SN ejecta, mostly owing to the ease with which Compton scattering may be treated in a Monte Carlo scheme (see e.g. Milne et al. 2004 for discussion of SN Ia γ-ray transport or Pozdniakov et al. 1983 for an extensive review of Comptonization). They are also highly effective for following radiation transport in SNe Ia beyond the γ-regime, thereby obtaining bolometric light curves (following Cappellaro et al. 1997) and even time-series spectra (Mazzali & Lucy 1993; Kasen et al. 2006).

The code used here (Sim 2007) is closely based on the scheme and test code developed by Lucy (2005). We briefly summarise its operation and describe the physical processes included. We then describe how the histories of the quanta are used to deduce volume based emissivities for computation of the emergent γ-ray spectra.

2.1 Overview of code operation

As described by Lucy (2005), the Monte Carlo quanta used in our code represent indivisible parcels of energy. They begin as pellets of radioactive material which were synthesised during nucleosynthesis in the first few seconds of the SN explosion.

These pellets decay according to the radioactive nuclei they represent and are converted into γ-ray packets. The initial frequencies of these γ-rays are chosen by sampling the relative probabilities of the different emission lines that arise from radioactive decay.

The propagation of the γ-rays is followed in 3D space, time and photon frequency until they either escape from the SN or are lost from the γ-ray regime; the latter can occur as a result of energy loss to non-thermal electrons in Compton scattering or by photoabsorption. During the Monte Carlo simulation, the trajectories of the quanta are used to compute volume-based emissivities; the final spectra are obtained from a formal solution of the radiative transfer equation using these emissivities (see Section 2.5).

Typically, 4×10^7 quanta are used in each Monte Carlo simulation. They are tracked on a homologously expanding 100^3 Cartesian grid. The simulations cover the time interval 5 – 150 dy which is discretised into 50 logarithmically spaced steps.

2.2 Radioactive emission

In the calculations, only ^{56}Ni and ^{56}Co are included as sources of γ-ray emission. The relevant nuclear data are taken from Ambwani & Sutherland (1988); their Table 1. All the ^{56}Ni is assumed to be produced in the first seconds of the explosion (i.e. at $t = 0$, for our purposes); ^{56}Co is produced only as a result of the subsequent decay of ^{56}Ni (i.e. no ^{56}Co is directly synthesised).

Following Ambwani & Sutherland (1988) and Lucy (2005), positrons released by ^{56}Co decays are assumed to decelerate rapidly and then annihilate in situ, leading to the emission of two 0.511 MeV γ-ray photons in the local comoving frame (i.e. we adopt a positronium fraction of zero; see e.g. Milne et al. 2004 for a discussion). The kinetic energy deposited in the deceleration is assumed to be radiated at much softer energies and not to contribute to the γ-ray spectrum.

Although other radioactive isotopes are synthesised in the early stage of a SN explosion (e.g. ^{44}Ti, ^{57}Ni and ^{57}Co), they are expected to have much smaller mass fractions than ^{56}Ni (see e.g. Travaglio et al. 2004) and can be neglected at relatively early times (i.e. when the light curves are bright and dominated by ^{56}Ni and ^{56}Co). All other sources of γ-ray emission (e.g. nuclear excitation or spallation) are neglected because, as discussed by Gómez-Gomar et al. (1998), their contributions are negligible until very late times.

2.3 Scattering

The most important physical process the γ-ray quanta undergo is Compton scattering. It is treated via the indivisible-energy-packet scheme presented by Lucy (2005). The Compton cross-section (σ_C) is given as a function of photon energy and scattering angle by the Klein-Nishina formula. In all calculations, we neglect the initial electron momentum in the comoving frame.

2.4 Absorption

Two γ-ray destruction processes are included in the calculations. First, photoabsorption is included following Lucy (2005). The photoabsorption cross-section per unit gram ($\kappa_{ph}(E)$) is allowed to depend on composition in a simple manner:

$$\kappa_{ph}(E) = X_{\text{Fe-grp}}\ \kappa_{28}(E) + (1 - X_{\text{Fe-grp}})\ \kappa_{14}(E) \qquad (1)$$

where $X_{\text{Fe-grp}}$ is the local mass fraction of iron-group elements and $\kappa_{28}(E)$ and $\kappa_{14}(E)$ are the photoabsorption cross-sections per gram typical of high-and intermediate-mass elements, respectively (the subscripts refer to the "typical" atomic mass number, Z). Specific expressions for $\kappa_{28}(E)$ and $\kappa_{14}(E)$ are obtained from Veigele (1973) following Ambwani & Sutherland (1988).

Second, for γ-rays above 1.022 MeV, pair production is included. The cross-section for this process, $\kappa_{pp}(E)$, is allowed to depend on composition in the same way as photoabsorption (Equation 1). The representative cross-sections for intermediate- and high-mass elements ($Z = 14$ and 28) are obtained using equation 2 of (Ambwani & Sutherland 1988).

When a pair production event occurs, probabilities are assigned to determine whether the outcome is a positron or a non-thermal-electron packet (see Lucy 2005). The kinetic energy of both positron and electron are assumed to be lost from the γ-ray regime. However, as with the positrons emitted by ^{56}Co, the positrons resulting from pair-creation are assumed to annihilate in situ, leading to the emission of two γ-rays at 0.511 MeV.

2.5 Extraction of spectra

As discussed by Lucy (1999, 2003, 2005), and in the context of the current code by Sim (2007), optimal use of a Monte Carlo simulation of radiation transport is generally obtained by recording volume based estimators and using these to extract the quantities of interest. The estimators required are those from which we obtain the Compton emissivity (η^C, a function of position, time,

frequency and observer line-of-sight direction) and the 0.511 MeV-emissivity arising from pair-production (η^{pp}). With these emissivities known, a formal solution of the radiative transfer equation can be performed to deduce the spectrum (see Lucy 1999; Sim 2007). The third emissivity term required for the formal solution – describing direct γ-ray emission from radioactive decay – does not require a Monte Carlo estimator since it can be derived from the assumed distribution of radioactive material.

Monte Carlo estimators for η^C are recorded in every grid cell during all relevant time steps in the simulation, on a pre-determined frequency grid. In the comoving frame

$$\eta^C_{\rm cmf} = \frac{n_e}{V\ \Delta t\ \Delta\nu} \sum_{\gamma\text{-paths}} \frac{\epsilon_{\rm rf}}{f} {\rm d}s (1 - 2\boldsymbol{v}\cdot\hat{\boldsymbol{n}}/c) \left(\frac{{\rm d}\sigma}{{\rm d}\Omega}\right)_{\nu_{\rm cmf},\mu_{\rm cmf}} \quad (2)$$

where the summation runs over all γ-ray trajectories inside the grid cell during the time step; ${\rm d}\sigma/{\rm d}\Omega$ is the Klein-Nishina differential cross-section, evaluated at the comoving frequency of the γ-ray packet ($\nu_{\rm cmf}$) and for a scattering angle specified by $\mu_{\rm cmf}$ (the cosine of the comoving-frame angle between the direction of packet propagation and the observer line-of-sight); $\boldsymbol{v}$ is the ejecta velocity, $\hat{\boldsymbol{n}}$ the rest-frame direction in which the packet is propagating, $\epsilon_{\rm rf}$ the rest-frame packet energy and ds the trajectory length; f is the ratio of photon energies before and after Compton scattering

$$f = 1 + \frac{h\nu_{\rm cmf}}{m_e c^2}(1 - \mu_{\rm cmf}) \ ; \quad (3)$$

n_e is the electron number density, V is the volume of the grid cell, Δt the duration of the time step and $\Delta\nu$ the width of the frequency bin. The frequency bin to which a given γ-ray trajectory is assigned is determined by $\nu_{\rm cmf}/f$, the comoving frame frequency hypothetical photons from the γ-packet would have were they to undergo Compton scattering into the observer line-of-sight.

The corresponding estimator for η^{pp} is simpler. Since the emission is restricted to a single comoving-frame photon energy (0.511 MeV), only one estimator per grid cell per time step is required for this process; it is given by

$$\eta^{pp}_{\rm cmf} = \frac{1}{4\pi V\ \Delta t} \sum_{\gamma\text{-paths}} \epsilon_{\rm rf}\ \frac{2m_e c^2}{h\nu_{\rm cmf}}\ {\rm d}s\ (1 - 2\boldsymbol{v}\cdot\hat{\boldsymbol{n}}/c)\ \kappa_{pp}\ . \quad (4)$$

The summation now runs over all γ-trajectories in the cell during the time step and for which the photon energy is above the pair-creation threshold. Although $\eta^C_{\rm cmf}$ is a specific emissivity, $\eta^{pp}_{\rm cmf}$ is not – hence they differ dimensionally by [Hz^{-1}]. Throughout this study it is assumed that emission-line shapes are determined by the macroscopic velocity field. Thus the intrinsic emission profile associated with $\eta^{pp}_{\rm cmf}$ is taken to be arbitrarily narrow.

All the spectra shown in this paper were computed via formal solutions of the radiative transfer equation using the Monte Carlo emissivity estimators given above. The accuracy and validity of the use of the estimators was separately tested by comparing spectra obtained from the formal solution with those obtained by direct frequency binning of emergent Monte Carlo quanta for our spherically symmetric "control" model (Model SC, see below). To the level of the Monte Carlo noise in the frequency-binned spectrum (typically a few percent), the two methods produced indistinguishable results, as expected.

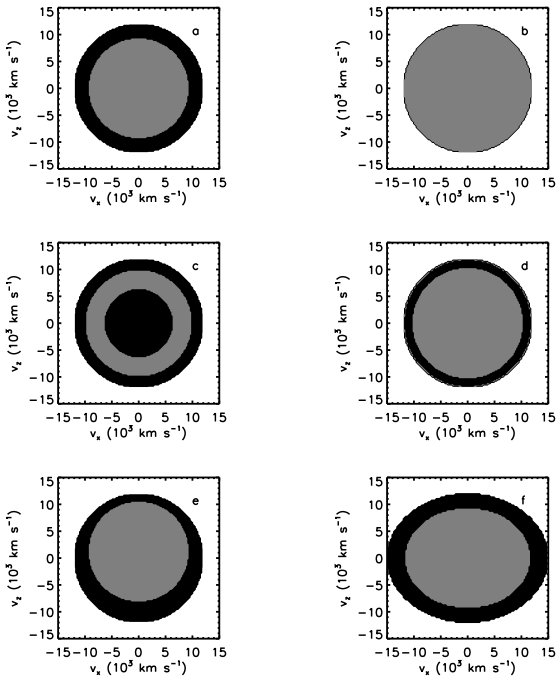

Figure 1. Slices through the x-z velocity-space plane showing the distribution of ^{56}Ni adopted in the models. Grey indicates regions which initially contain ^{56}Ni while black shows the volumes that do not. Panel a shows the basic geometry used for Models SC, SS and SFeR. Panels b, c, d, e and f show, respectively, Models SM, SFeC, SNiS, AO and AE. All models are symmetric under rotation about the z-axis.

3 MODELS

We computed γ-ray radiation transport for a set of eight models. These are not tied to specific progenitor/explosion scenarios in detail but are all rooted in previous discussions of SNe Ia.

Although quite diverse, our models are not remotely exhaustive of all possible conditions or geometries. However, as stated in Section 1, our intention is not to address specific explosion models but to explore whether relatively model-independent information can be inferred from the γ-ray regime.

Compared to other spectral regions (e.g. ultraviolet, optical, infrared etc.), the γ-ray spectrum is comparatively simple – its brightness and shape are mainly determined by only two quantities: the instantaneous number of radioactive decays and the optical depth to Compton scattering (τ_C). Thus to first order, γ-ray data constrain only the properties that are relevant to these two quantities. Of course, other processes (e.g., photoabsorption) have a role in establishing the γ-ray spectrum, but their effects are generally secondary and they may be disentangled.

The most easily understood parameter for γ-ray emission is the total mass of radioactive material ($M_{\rm Ni}$). Except for two cases (see below), we fix this at 0.6 M$_\odot$. To zeroth-order, a larger mass leads to brighter emission. However, there are additional effects.

A second relevant quantity is the velocity distribution of ^{56}Ni since Doppler shifts are important in setting emission line widths (see e.g. Milne et al. 2004). Detailed radiation transport is not really needed to explore this simple relationship, particularly since only extremely sensitive observations could constrain line profiles (see e.g. Gómez-Gomar et al. 1998).

Radiation transport *is* important for the shape of both the

light curve and the spectrum. The dominant process affecting γ-ray transport in SNe Ia is Compton scattering. Neglecting light travel time effects and relativistic corrections, τ_C is sensitive only to the column density of target electrons (N_e). Since the photon energies under consideration ($\sim$ 1 MeV) are very large compared to the binding energies of electrons in atoms (typically in the 10 eV – 10 keV range), it is reasonable to regard all electrons as available Compton-targets. Thus the Compton optical depth is independent of the thermal, ionization and excitation states of the plasma and, to a good approximation, also of the density profile along the line-of-sight since both the velocity and the velocity gradient appear only through Doppler factors. This is in contrast to other wavebands (e.g. the optical) where line opacity dominates giving greater significance to the velocity structure.

In light of these considerations, our models explore a wide range of distributions of radioactive source material with τ_C – as a minimal standard of data quality, this distribution should be constrained before data can support or exclude any specific scenario.

Six of our models are spherically symmetric while the other two are aspherical. As mentioned in Section 1, most previous studies of γ-ray spectra were restricted to 1D calculations. In one of the few multi-dimensional studies of SN Ia γ-ray spectra, Höflich (2002) considered an elliptical SN explosion and showed that significant viewing angle effects may occur, particularly at relatively early times. That result is comparable to those from studies of aspherical SNe Ia in other wavebands (e.g. Höflich 1991; Kasen & Plewa 2006; Sim et al. 2007; Hillebrandt et al. 2007) which show that viewing angle effects are potentially observable and could be confused with other phenomena. Therefore, one of our objectives is to add aspherical models to the zoo of other possibilities and consider whether they could be distinguished.

The eight models we use are described below. They are labelled by two to four letters – the first letter identifies whether the model is spherical ("S") or aspherical ("A") while the others abbreviate the model properties. The model geometries are shown in Fig. 1. All models are assumed to be in homologous expansion and, for simplicity, to have uniform mass-density (as noted above, the density profile is relatively unimportant for the synthesis of the γ-ray spectrum).

3.1 Model SC: control model

Our first model, which we use as the standard of comparison for all the others, is spherically symmetric with a total mass $M_{\rm T} = 1.4$ M$_\odot$ and $M_{\rm Ni} = 0.6$ M$_\odot$. The maximum ejecta velocity is set at $v_{\rm max} = 1.2 \times 10^9$ cm s^{-1}. This is lower than the maximum velocities in real SNe but representative of the velocity regime in which the density is large and is therefore appropriate given our choice of a uniform density profile (see above). In this model, the ^{56}Ni is located in a spherical region at the centre of the ejecta. The volume of this region is fixed by an adopted ^{56}Ni mass fraction of 0.9. The region outside the central concentration of Ni is assumed to be composed of intermediate mass elements.

3.2 Model SS: super-Chandrasekhar mass model

Model SS has the same geometry and Ni-distribution as Model SC but its densities are everywhere higher by a factor of 1.5. Thus, this model is "super-Chandrasekhar", having $M_{\rm T} = 2.1$ M$_\odot$ and $M_{\rm Ni} = 0.9$ M$_\odot$. This model explores γ-ray emission from objects in which τ_C is higher than in Model SC. Although outside the standard SN Ia paradigm, Super-Chandrasekhar explosions have been proposed for unusually bright events such as SN 1991T (Fisher et al. 1999), SN 2003fg (Howell et al. 2006) and SN 2006gz (Hicken et al. 2007).

3.3 Model SFeR: Fe-rich ejecta

This model isolates the effect of composition. It adopts the same geometry, mass and Ni-distribution as Model SC. However, it assumes that the majority of the material that is not initially ^{56}Ni consists of other heavy nuclei; the photoabsorption and pair-production cross-sections are thus different from Model SC.

3.4 Model SM: well-mixed model

This model is identical to Model SC ($M_{\rm T} = 1.4$ M$_\odot$, $M_{\rm Ni} = 0.6$ M$_\odot$) except that ^{56}Ni is distributed uniformly throughout the volume of the ejecta (see panel b of Fig. 1).

3.5 Model SFeC: stable Fe core

Recently, Mazzali et al. (2007) have argued for a model which may account for most SNe Ia. Analysing spectra of a large sample of SNe, they concluded that the characteristic structure consists of a low-velocity core of stable iron-group material surrounded by a ^{56}Ni-rich region. Outside this region, the material underwent incomplete nuclear burning and is dominated by intermediate-mass nuclei. Motivated by their study, we include a model based on such a structure (the geometry is shown in panel c of Fig. 1). The inner stable iron-group core has a mass of 0.2 M$_\odot$. A pure ^{56}Ni-region lies immediately above this core and contains 0.6 M$_\odot$. The outermost region is composed of intermediate-mass elements only.

3.6 Model SNiS: Ni-rich core and surface layer

This model differs from all others as it includes two physically separated ^{56}Ni-rich regions: a massive core and a thin surface layer. This geometry provides an alternative to the "super-Chandrasekhar" scenario (see Section 3.2) for unusually bright events. For this model we retain $M_{\rm T} = 1.4$ M$_\odot$, adopt a core ^{56}Ni-mass of 0.9 M$_\odot$ and assume that the outermost 0.1 M$_\odot$ of the ejecta is also pure ^{56}Ni. This outer layer is motivated by the early-time spectroscopic behaviour of SN1991T (Mazzali et al. 1995). The material sandwiched between the core and the outer Ni-rich shell is taken to be composed of intermediate mass elements. This model has the largest $M_{\rm Ni}$ in our study, as required to account for the brightness of events such as SN1991T.

3.7 Model AO: off-set Ni

Here, the basic model is identical to Model SC but the centre-of-mass of the Ni ball is displaced along the z-axis by 10 per cent of the outer ejecta radius. This leads to an aspherical model, very similar to those discussed by Sim et al. (2007).

3.8 Model AE: ellipsoidal ejecta

In this model, the maximum ejecta velocity varies with direction, producing an ellipsoidal SN. This is the same basic geometry as considered by Höflich (2002). Ellipsoidal explosions have been suggested following detection of polarisation in SNe Ia (e.g.

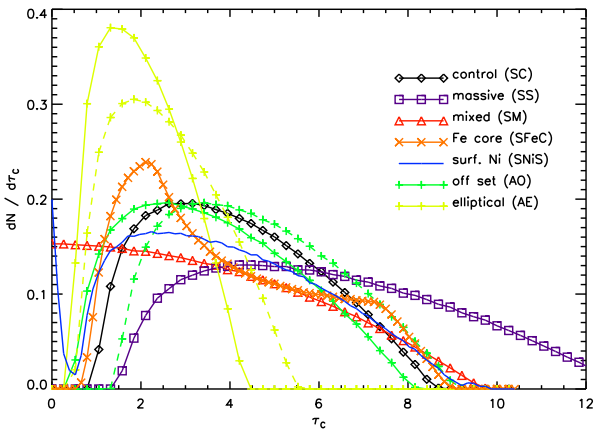

Figure 2. Distribution of source ^{56}Ni with electron scattering optical depth (computed in the Thompson limit) for the models. The distribution is normalised to $\int_0^\infty \frac{\mathrm{d}N}{\mathrm{d}\tau_C}\,\mathrm{d}\tau_C = 1$. The symbols are indicated in the figure. Model SFeR is not plotted since, with respect to this distribution, it is identical to Model SC. For both the aspherical models (Models AO and AE), two curves are plotted – these represent the extremes with respect to viewing angle: for Model AO, the solid line is for a line-of-sight parallel to the direction in which the Ni-blob is displaced from the centre of the SN while the dashed line is for the anti-parallel light-of-sight; for Model AE, the solid line is for viewing down the short axis of the ellipsoid while the dashed line is for a line-of-sight along the long axis.

Howell et al. 2001; Wang et al. 2003). The maximum velocity (1.5×10^9 cm s^{-1}) occurs at the equator. The axis ratio is set to 5:4; therefore the terminal velocity of the ejecta in the polar direction is 1.2×10^9 cm s^{-1}. The Ni-distribution is ellipsoidal in the same sense as the total mass distribution and remains centrally concentrated. As in all the other models, the mass-density remains uniform.

3.9 Distribution of emission with opacity

As discussed above, since the γ-ray spectrum is primarily determined by Compton scattering, we expect that a highly relevant quantity is the distribution of ^{56}Ni with τ_C (see Fig. 2). τ_C is a decreasing function of both time and photon energy. However, since the energy dependence is universal and, in an homologous flow, the time dependence is very simple ($\tau_C \propto t^{-2}$), it is sufficient to compare the distribution for one photon energy at one time. For convenience, the optical depths used in Fig. 2 are computed using the Thompson limit to σ_C at time $t = 50$ dy.

Fig. 2 shows that the models considered *are* quite diverse and reasonably complete, covering a range of plausible single-peaked distributions. At the epoch considered, the radioactive material in Model SC is concentrated at moderate optical depths, and its distribution is bracketed by the extremes shown in Model AO. Models SFeC and AE have lower optical depths, but their distributions are still peaked significantly away from $\tau_C = 0$. Model SM has an extreme distribution, with a significant fraction of the source material at very low optical depths ($\tau_C \sim 0$). At the opposite limit, Model SS has higher opacities, resulting from the larger density. Model SNiS differs from the others in having two peaks in its distribution – most of the Ni lies at moderate optical depths but the thin surface layer provides a distinct peak at very low optical depth.

Model SFeR is not shown in Fig. 2; its distribution of ^{56}Ni with τ_C is identical to Model SC so that it can isolate the signatures of photoabsorption.

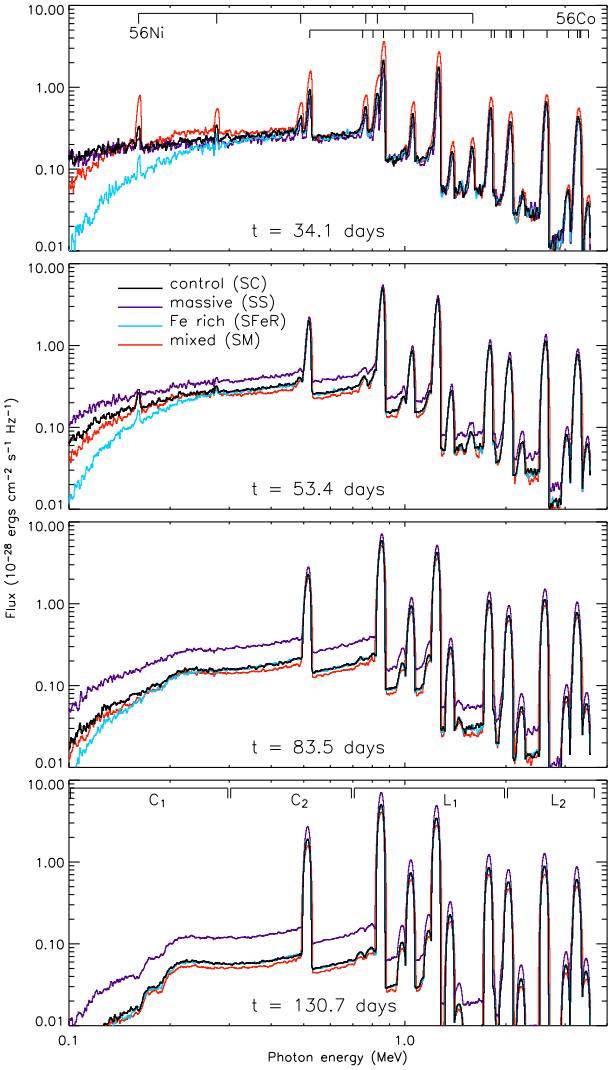

Figure 3. Representative time series of γ-ray spectra computed with four spherically symmetric models (identified in the second panel) at times after explosion as indicated on each panel. The ^{56}Ni and ^{56}Co emission lines are identified in the top panel. The four flux-bands discussed in Section 5.3 are indicated in the bottom panel. Fluxes are for a source distance of 1 Mpc.

4 DISCUSSION OF SPECTRA

Fig. 3 shows a time series of spectra computed from Model SC and spectra from three other spherical models (SS, SFeR and SM) are over-plotted. (For clarity, spectra from the remaining four models are not plotted. They are, however, included in all the discussions of observable diagnostics in subsequent sections.)

At times close to maximum light the γ-ray spectrum consists of strong emission lines, mainly due to ^{56}Co, with significant continuum arising from Compton scattering of line photons. Since optical depths decrease with time in the expanding ejecta, the strength of the lines relative to the continuum increases with time. At early times, the "mixed" model (Model SM) shows a harder continuum than the standard model and stronger Ni emission lines (particularly

0.158 MeV and 0.275 MeV). These lines are also fairly strong in Model SNiS (not plotted) where they originate in the surface layer of ^{56}Ni. As noted by Gómez-Gomar et al. (1998), these Ni lines can only form when the source Ni lies at small τ_C; since σ_C decreases with increasing photon energy, the soft-energy lines are degraded most easily, becoming swamped by photons down-scattered from harder energies.

In Model SS, the 0.158 and 0.275 MeV lines are almost completely buried by the strong continuum which persists until well after maximum light as a consequence of the high τ_C's in this model.

Model SFeR shows the effect of composition as intended. Above about 0.3 MeV, its spectra are indistinguishable from those of Model SC. At soft energies, however, the Model SFeR flux is lower by up to an order of magnitude. This is due entirely to the difference in the photoabsorption cross-section arising from the choice of composition. Although weaker, a similar effect appears in Model SNiS because of the relatively large amounts of iron-group material in that model, particularly in the surface layer.

Should energy-resolved data of sufficient sensitivity to measure both the line and continuum emission across the entire 0.1 – 3.5 MeV spectrum be obtained, it would be used to evaluate SN models by direct comparison. However, given the rarity of very nearby SNe Ia and the limited sensitivity of γ-ray observatories, in the next section we will consider what information could be extracted from low quality γ-ray data in the form of simple diagnostics. We will focus on line and continuum fluxes. Although the energy resolution of γ-ray instruments can be high enough to resolve spectral lines (e.g. with *SPI Integral*, see Roques et al. 2003), sensitivity limits make it practically impossible to measure detailed line shapes except for extremely nearby events (Gómez-Gomar et al. 1998).

5 OBSERVATIONAL DIAGNOSTICS

We consider three different potential diagnostics that could, in princple, be obtained from γ-ray data. Throughout our discussion, we use theoretical source count rates to illustrate the value of the diagnostics for distinguishing our models. We do not, however, consider any additional effects (e.g. instrumental noise) which would make detections much harder with current observatories (see e.g. Gómez-Gomar et al. 1998).

We begin with the simplest diagnostic, the energy-integrated light curve.

5.1 γ-ray light curves

5.1.1 Discussion

The γ-ray light curve is the most useful for constraining $M_{\rm Ni}$ since in this spectral region the decay products of ^{56}Ni and its daughter nucleus ^{56}Co are seen most directly.

Fig. 4 shows energy-integrated (0.1 – 3.5 MeV) light curves from the models. All the light curves have a characteristic, single-peaked shape. They peak later ($t_{\rm peak} = 50$ – 80 dy) and are simpler in shape than model bolometric (or optical/infrared) light curves (see e.g. Blinnikov et al. 2006; Kasen et al. 2006; Kasen 2006; Kasen & Woosley 2007) since photon trapping plays a far less significant role in the γ-ray regime.

After about 100 dy, all our models are fairly optically thin and the γ-ray luminosity is an unambiguous measure of $M_{\rm Ni}$ via

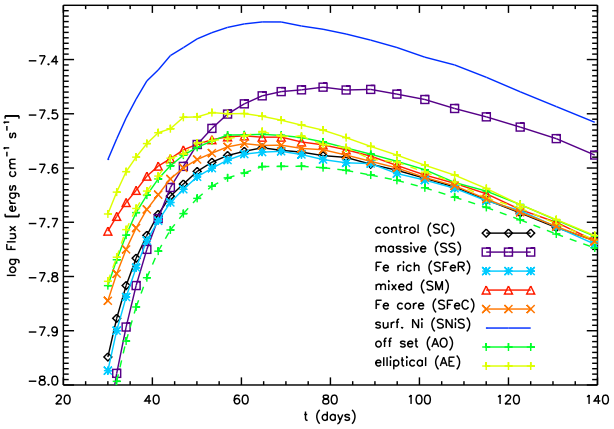

Figure 4. Model light curves for the 0.1 – 3.5 MeV γ-ray region. The flux is given for a source distance of 1 Mpc. Times are measured from the explosion. For the aspherical models (AO and AE), two curves are plotted – as in Fig. 2, these represent the extremes with respect to viewing angle.

$$L_\gamma(t \gtrsim 100\ dy) \approx \epsilon_{\rm Co} M_{\rm Ni} \exp(-t/t_{\rm Co})/t_{\rm Co} \approx 1.23 \times 10^{43} \frac{M_{\rm Ni}}{M_\odot} \exp(-t/t_{\rm Co})\ \ {\rm ergs\ s^{-1}} \quad (5)$$

where $L_\gamma(t)$ is the emitted γ-ray luminosity, $\epsilon_{\rm Co}$ is the total γ-ray energy released during the decay of one gram of ^{56}Co and $t_{\rm Co}$ is the ^{56}Co lifetime. In Fig. 4, this optically-thin behaviour causes the light curves of all models with the same adopted $M_{\rm Ni}$ (SC, SFeR, SM, SFeC, AO and AE) to converge for $t > 100$ dy while models with higher $M_{\rm Ni}$ (SS and SNiS) are proportionally brighter.

At earlier times, individual model light curves differ significantly – the spread is about a factor of two at $t \sim 40$ dy. The light curves of models containing Ni at relatively low τ_C (SM, AE, SNiS, SFeC and face-on AO; see Fig. 2) tend to rise quickly and peak early but the light curve shapes are different and do not adhere to a one-parameter family. The aspherical models show viewing angle dependence of up to 50 per cent at early times, decreasing to about 10 – 20 per cent at $t_{\rm peak}$ which is comparable to differences between our various spherically symmetric models.

The integrated light curve is almost insensitivity to photoabsorption (in Fig. 4, compare Models SFeR and SC) – most of the γ-rays are too hard for significant photoabsorption to occur, regardless of the composition of the absorbing material.

5.1.2 Diagnostic value

With good time coverage (40 – 120 dy after explosion), the γ-ray light curve alone can provide useful information: at late times it gives the most direct measurement of $M_{\rm Ni}$ while at earlier stages it is sensitive to the distribution of τ_C (i.e. electrons and therefore total mass).

To assess the diagnostic value of a SN Ia γ-ray light curve, we converted our theoretical light curves to source counts. For illustrative purposes, we used the energy-dependent effective area of *Integral SPI* (Attié et al. 2003; Diehl et al. 2003; Sturner et al. 2003), adopted a distance of 18 Mpc to the SNe (an approximate distance to the Virgo cluster, Fouqué et al. 2001) and assumed an integration time of 10^5 s (~ 1 dy). Under these conditions Model SC would give ~ 460 photon counts at $t \sim 50$ dy, decreasing to ~ 310 counts at $t \sim 100$ dy.

Therefore, if photon counting statistics were the only limitation, it would be quite feasible to deduce SN Ia ^{56}Ni-masses to a precision of about 10 per cent for objects at distances up to Virgo. Some rough information on the light curve shape between about 40 and 100 dy after the explosion could also be obtained. The level of precision would be comparable to the typical differences between the models investigated here, so that a time sequence of data could place fairly robust constraints not only on the total ^{56}Ni mass, but also on its distribution with opacity.

Of course, these estimates are very crude and optimistic since additional sources of error (e.g. background) have not been considered, but they do suggest that, in principle, useful information is contained in light curve data.

5.2 Line ratios

5.2.1 Discussion

γ-ray emission line peak-intensity ratios provide simple diagnostics (Burrows & The 1990; Höflich et al. 1998; Gómez-Gomar et al. 1998). As in earlier studies, we examine only a few lines and their ratios in detail. Owing to the simplicity of spectral formation in the γ-ray regime, exactly which lines are considered is fairly unimportant – the qualitative behaviour of any line ratio will be similar to that of one of those we show.

Since the strongest lines originate in the decay of ^{56}Co, their intrinsic relative strengths are set by nuclear physics alone – thus late-time measurements of line ratios yield no information that cannot be gleaned from the energy-integrated light curve. However, at early times, the energy sensitivity of σ_C makes the intensity ratio of lines at different energies sensitive to N_e (Höflich et al. 1998).

The left panel of Fig. 5 shows the ratio $R_1 = F(0.847 \text{ MeV})/F(2.598 \text{ MeV})$. Both lines in this ratio are from the decay of ^{56}Co. We chose to consider this particular pair of lines since they are strong, unblended and well-separated in energy. Although an even more widely spaced pair of lines associated with ^{56}Co could be achieved considering the 0.511 keV positron-annihilation line, we prefer to avoid reliance on our adopted positronium fraction. The R_1 ratio in Fig. 5 has been normalised such that it tends asymptotically to 1.0 in the optically thin limit.

For times up to about 70 dy, R_1 discriminates between different distributions of ^{56}Ni with τ_C (see Fig. 2). Using this ratio, spherical models in which the radioactive material is behind most opacity (Model SS) and least opacity (Model SM) can be easily discriminated from the control model. Aspherical models behave similarly – in Model AO, R_1 is largest if observed from the side to which the Ni blob is displaced; the effect is present but weaker in Model AE because τ_C is typically smaller.

As for R_1, for any other pair of strong Co emission lines the flux ratio $F(\epsilon_1)/F(\epsilon_2)$ will be determined by the ratio of Compton opacity at the two line energies, $\sigma_C(\epsilon_2)/\sigma_C(\epsilon_1)$. We will not discuss these other potential diagnostic ratios but only comment that the most useful ratios will always be those between lines of significantly different energy (as in R_1). Thus, the ratio of the two strongest lines ($F(0.847 \text{ MeV})/F(1.238 \text{ MeV})$), although easier to measure, has less diagnostic value than R_1.

The second line-flux ratio shown in Fig. 5 is between the ^{56}Ni 0.158 MeV line and the ^{56}Co 0.847 MeV line, referred to as R_2. In the figure, it is normalised to the optically thin limit, a decreasing function of time set by the decay rates of ^{56}Ni and ^{56}Co.

For most models, R_2 gives the same relative ordering as R_1 at early times. Again, this is primarily due to the energy-dependence of σ_C. However, the effect is weaker in R_2 than R_1 because it is opposed by an increase in the Compton continuum flux around 0.158 MeV. Disentangling these two effects would require sufficiently high quality data that the γ-ray continuum level around the 0.158 MeV line can be measured.

Unlike R_1, however, R_2 effectively separates Model SFeR from any of the others at $t < 50$ dy since the 0.158 MeV line is sufficiently soft to be affected by photoabsorption. Thus, in agreement with Gómez-Gomar et al. (1998), we conclude that R_2 (or an equivalent ratio of one of the low-energy Ni lines to a harder Co line) provides an important diagnostic for composition.

5.2.2 Diagnostic value

The R_1 and R_2 ratios defined above provide useful diagnostics for two of the quantities that may be constrained via the γ-ray spectrum, the distribution of total mass and the composition of the photoabsorbing plasma.

Peak count rates for the relevant emission lines computed adopting the same conditions described in Section 5.1.2 are shown in Fig. 6. For both the 0.158 and 0.847 MeV lines, the peak count rates are several thousand/MeV. The intrinsic line widths, determined by the velocity range in the ejecta, are $\sim$ 6 keV for the 0.158 MeV line and $\sim$ 34 keV for the 0.847 MeV line. These widths are large enough to be moderately well-resolved by modern instruments (Attié et al. 2003; Roques et al. 2003). For our assumed distance and integration time, one would only expect around 50 source counts in the 0.847 MeV line and fewer than 10 source counts in the 0.158 MeV line.

Owing to the combination of fewer source photons and smaller adopted detector effective area, there are fewer counts/MeV for the 2.598 MeV line – only a handful of counts integrated over the line profile.

Thus, statistical errors caused by small number counts are very substantial in both R_1 and R_2, meaning that these ratios could not contain useful information for objects at our chosen distance. A tenfold increase in source counts would be needed to make the statistical accuracy comparable to any of the differences between the models (as shown in Fig. 5). With 50 – 100 times more counts and good time coverage these ratios could contain detailed information although additional instrumental effects would further limit their value in practise.

In light of this difficulty, in the next section we consider an alternative approach in which the spectrum is coarsely binned and hardness ratios are extracted.

5.3 Hardness ratios

5.3.1 Discussion

Given the simplicity of the γ-ray spectrum, moderately complete information can be obtained from hardness ratios alone; this is in contrast to other wavebands where spectra are complex and not well-described by photometry alone. Some prospects of using relatively broad energy bands for probing the soft, continuum regions of the spectrum were discussed by Gómez-Gomar et al. (1998). We extend this to consider hardness ratios involving both continuum-dominated and higher energy line-dominated bands.

We have divided the spectrum into four energy bands, two in which the Compton continuum contributes significantly to the flux (C_1 and C_2) and two in which strong line emission always domi-

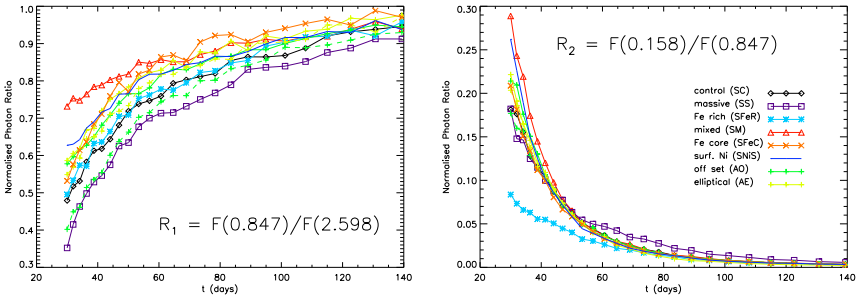

Figure 5. Peak line flux ratios from the various models as functions of time since explosion. The left panel shows the ratio $R_1 = F(0.847\ \mathrm{MeV})/F(2.598\ \mathrm{MeV})$ and the right panel $R_2 = F(0.158\ \mathrm{MeV})/F(0.847\ \mathrm{MeV})$. For the two aspherical models (Models AO and AE), two curves are plotted – as in Fig. 2, these represent the extremes with respect to viewing angle. Flux ratios are normalised to the optically thin limit (thus, the normalised R_1-ratio asymptotes to 1.0 while R_2 asymptotically approaches the instantaneous mass ratio of ^{56}Co to ^{56}Ni).

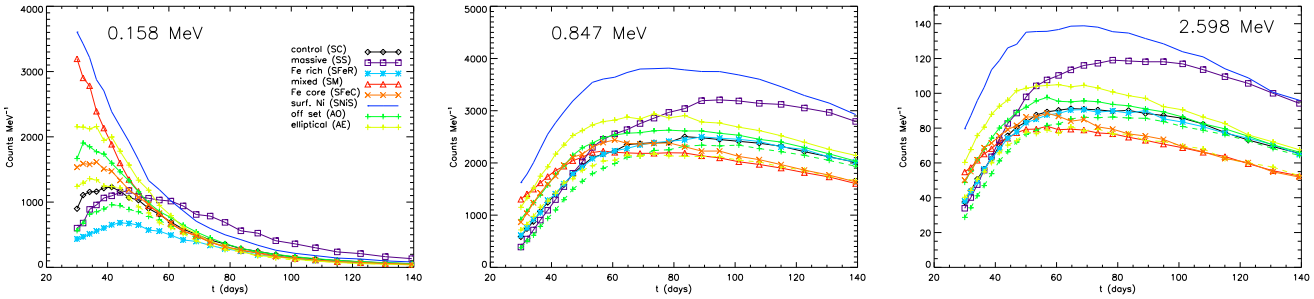

Figure 6. Predicted peak counts MeV^{-1} for the 0.158, 0.847 and 2.598 MeV emission lines computed adopting the *Integral SPI* effective area, a recording interval of 10^5 s and a source distance of 18 Mpc. For both the aspherical models (Models AO and AE), two curves are plotted – as in Fig. 2, these represent the extremes with respect to viewing angle.

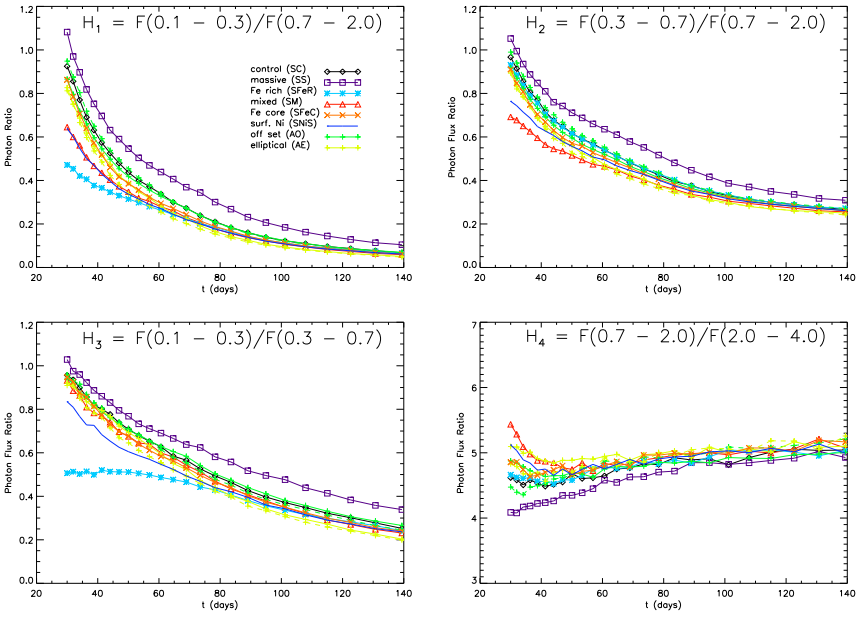

Figure 7. Hardness ratios computed from the various models as functions of time since explosion. For the aspherical models, two curves are plotted – as in Fig. 2, these represent the results for the two extreme observer lines-of-sight.

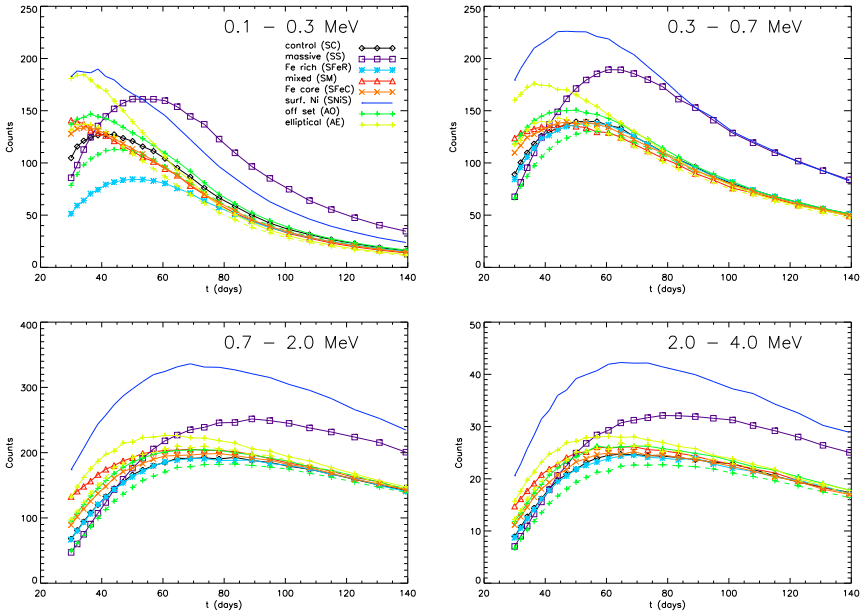

Figure 8. Synthetic light curves for the various models in each of the four energy bands considered computed adopting the *Integral SPI* effective area, a recording interval of 10^5 s and a source distance of 18 Mpc. For the aspherical models, two curves are plotted – as in Fig. 2, these represent the results for the two extreme observer lines-of-sight.

nates (L_1 and L_2). The bands are defined below and are indicated in Fig. 3:

- C_1 (0.1 – 0.3 MeV): emission is generally dominated by Compton down-scattering of harder photons, photoabsorption can be significant.
- C_2 (0.3 – 0.7 MeV): emission is predominantly through Compton down-scattering. There is some direct line emission, mostly via the 0.511 MeV electron-positron annihilation line.
- L_1 (0.7 – 2 MeV): emission is dominated by strong lines of Co supplemented by a moderately weak Compton continuum.
- L_2 (> 2 MeV): lines of Co again dominate, now with an even weaker Compton continuum.

The line ratios R_1 and R_2 (see Section 5.2), are affected by the change in σ_C between different energies. A similar effect can be anticipated in the hardness ratio between the two line-dominated bands (L_1 and L_2) – such an effect is present but weak (see below). Another effect, however, can be noted when comparing fluxes at soft energies. The strength of the Compton continuum relative to the lines increases with opacity and thus high optical depths lead to softer hardness ratios when C_1 or C_2 are involved.

This is illustrated in Fig. 7 which shows four hardness ratios computed with different combinations of the four γ-ray bands. The hardness ratios $H_1 = C_1/L_1$, $H_2 = C_2/L_1$ and $H_3 = C_1/C_2$, all show the effect of high τ_C in softening the spectrum. Of these, H_1 and H_2 are best at distinguishing the models, although the scale of the differences is smaller than in the line ratios (c.f. Fig. 5).

The hardness ratios involving the C_1 band (H_1 and H_3) are sensitive to the composition of the scattering material – these ratio clearly separate Model SFeR from Model SC. This behaviour is analogous to that of the R_2 line ratio.

The fourth ratio, $H_4 = L_1/L_2$ shows an opposite trend – it is hardest when optical depths are high (Fig. 5). As mentioned above, this can be understood by analogy to R_1 but H_4 is less sensitive since it represents an average over a range of energies.

Thus, γ-ray hardness ratios can contain quantitative information similar to that available from the line ratios discussed in Section 5.2. Although hardness ratios are less sensitive than line ratios, they may benefit from increased accuracy owing to the broad energy ranges over which the spectra can be integrated.

5.3.2 Diagnostic Value

Light curves of the various models in each of the four energy bands defined in Section 5.3.1 were computed, again adopting the same conditions described in Section 5.1.2, and are shown in Fig. 8.

In the three softer bands, we expect roughly 100 – 150 source counts from most models at ~ 40 dy with the adopted observation parameters, giving an optimistic estimate of ~ 15 per cent statistical error in H_1, H_2 and H_3. This is sufficient to separate the most different models – Models SC and SFeR could be distinguished via either H_1 or H_3 while Models SM and SS would be measurably different from each other and marginally distinguishable from Model SC. However, there is little prospect of using these ratios to find any of the effects of asphericity captured by Models AO and AE.

The predicted L_2-band source count rate is too low to allow the H_4-ratio to be useful – only a handful of counts are anticipated in L_2 for any of the models, a consequence of the reduction in both our adopted detector effective area and number of source photons at hard energies.

Still, hardness ratios could carry some diagnostic information. In contrast to the line-ratio diagnostics (Section 5.2.2), an increase in the count number by even a modest factor would allow fairly detailed analysis. An increase by a factor of ~ 10 – say as a result of a serendipitously nearby SN Ia – would reduce the source statistical error in the H_1, H_2 and H_3 ratios to less than 10 per cent. At this level of accuracy, these ratios would contain quantitatively useful information, particularly if their time evolution could be followed through the peak of γ-ray emission.

6 SUMMARY AND PROSPECTS

Using a Monte Carlo code we computed γ-ray spectra for a variety of models to explore whether unambiguous constraints could be obtained from γ-ray observations of SNe Ia. Two aspherical toy geometries (a lop-sided distribution of Ni and an ellipsoidal ejecta) show that moderate departures from sphericity can produce viewing-angle effects at least as significant as those due to variations of key parameters in 1D models. Thus γ-ray data could carry some useful constraints on possible geometries, but caution must be applied when evaluating its potential usefulness in distinguishing specific explosion scenarios.

Given the limited sensitivity of current γ-ray missions, we conclude, in agreement with previous studies (e.g. Gómez-Gomar et al. 1998), that there is little prospect for obtaining useful constraints from line-ratio diagnostics except for fortuitously nearby objects. Instead, we suggest that the best prospects are offered by hardness ratios. In particular, owing to the simplicity of the physics underlying the γ-ray spectrum, a simple ratio of the total emission in a hard energy, line-dominated part of the spectrum to a soft energy, continuum-dominated region could discriminate between our more extreme models. We also emphasise the value of obtaining multiple observations over a wide time period given the diagnostic power of the light curve shape. In planning future γ-ray missions, greater sensitivity at harder energies ($\gtrsim 2$ MeV) should be given high priority since several of the most potentially useful diagnostics (e.g. our R_1- and H_4-ratios) require measuring the hardest energies in the spectrum.

ACKNOWLEDGMENTS

PAM thanks C. Wunderer and B. P. Schmidt, and SAS acknowledges R. Kotak and A. Watts, for stimulating discussions. This research was supported in part by the National Science Foundation under Grant No. PHY05-51164.

REFERENCES

Ambwani K., Sutherland P., 1988, ApJ, 325, 820
Attié D. et al., 2003, A&A, 411, L71
Blinnikov S. I., Röpke F. K., Sorokina E. I., Gieseler M., Reinecke M., Travaglio C., Hillebrandt W., Stritzinger M., 2006, A&A, 453, 229
Burrows A., The L.-S., 1990, ApJ, 360, 626
Cappellaro E., Mazzali P. A., Benetti S., Danziger I. J., Turatto M., della Valle M., Patat F., 1997, A&A, 328, 203
Diehl R. et al., 2003, A&A, 411, L117
Fisher A., Branch D., Hatano K., Baron E., 1999, MNRAS, 304, 67
Fouqué P., Solanes J. M., Sanchis T., Balkowski C., 2001, A&A, 375, 770
Gamezo V. N., Khokhlov A. M., Oran E. S., Chtchelkanova A. Y., Rosenberg R. O., 2003, Science, 299, 77
Gómez-Gomar J., Isern J., Jean P., 1998, MNRAS, 295, 1
Hicken M., Garnavich P. M., Prieto J. L., Blondin S., DePoy D. L., Kirshner R. P., Parrent J., 2007, ArXiv e-prints, 709
Hillebrandt W., Niemeyer J. C., 2000, Ann. Rev. Astron. Astrophys., 38, 191
Hillebrandt W., Sim S. A., Röpke F. K., 2007, A&A, 465, L17
Höflich P., 1991, A&A, 246, 481
Höflich P., 2002, New Astronomy Review, 46, 475
Höflich P., Khokhlov A., Mueller E., 1992, A&A, 259, 549
Höflich P., Stein J., 2002, ApJ, 568, 779
Höflich P., Wheeler J. C., Khokhlov A., 1998, ApJ, 492, 228
Howell D. A., Höflich P., Wang L., Wheeler J. C., 2001, ApJ, 556, 302
Howell D. A. et al., 2006, Nature, 443, 308
Jordan G. I., Fisher R., Townsley D., Calder A., Graziani C., Asida S., Lamb D., Truran J., 2007, ArXiv Astrophysics e-prints
Kasen D., 2006, ApJ, 649, 939
Kasen D., Plewa T., 2006, ApJ submitted (astro-ph/0612198)
Kasen D., Thomas R. C., Nugent P., 2006, ApJ, 651, 366
Kasen D., Woosley S. E., 2007, ApJ, 656, 661
Kumagai S., Nomoto K., 1997, in Ruiz-Lapuente P., Canal R., Isern J., eds, NATO ASIC Proc. 486: Thermonuclear Supernovae Gamma-rays and X-rays from Type Ia supernovae. pp 515–+
Lucy L. B., 1999, A&A, 345, 211
Lucy L. B., 2003, A&A, 403, 261
Lucy L. B., 2005, A&A, 429, 19
Mazzali P. A., Danziger I. J., Turatto M., 1995, A&A, 297, 509
Mazzali P. A., Lucy L. B., 1993, A&A, 279, 447
Mazzali P. A., Röpke F. K., Benetti S., Hillebrandt W., 2007, Science, 315, 825
Milne P. A. et al., 2004, ApJ, 613, 1101
Müller E., Höflich P., Khokhlov A., 1991, A&A, 249, L1
Pozdniakov L. A., Sobol I. M., Siuniaev R. A., 1983, Astrophysics and Space Physics Reviews, 2, 189
Reinecke M., Hillebrandt W., Niemeyer J. C., 2002, A&A, 391, 1167
Röpke F. K., Gieseler M., Reinecke M., Travaglio C., Hillebrandt W., 2006, A&A, 453, 203
Röpke F. K., Hillebrandt W., 2005, A&A, 431, 635
Roques J. P. et al., 2003, A&A, 411, L91
Sim S. A., 2007, MNRAS, 375, 154
Sim S. A., Sauer D. N., Röpke F. K., Hillebrandt W., 2007, MNRAS, 378, 2
Sturner S. J. et al., 2003, A&A, 411, L81
Travaglio C., Hillebrandt W., Reinecke M., Thielemann F.-K., 2004, A&A, 425, 1029
Vedrenne G. et al., 2003, A&A, 411, L63
Veigele W. J., 1973, Atomic Data Tables, 5, 51
Wang L. et al., 2003, ApJ, 591, 1110
Winkler C. et al., 2003, A&A, 411, L1